Mechanisms of Severe Acute Respiratory Syndrome Coronavirus-Induced Acute Lung Injury

Lisa E. Gralinski,[a] Armand Bankhead III,[b] Sophia Jeng,[b] Vineet D. Menachery,[a] Sean Proll,[c] Sarah E. Belisle,[c] Melissa Matzke,[d] Bobbie-Jo M. Webb-Robertson,[d] Maria L. Luna,[d] Anil K. Shukla,[d] Martin T. Ferris,[e] Meagan Bolles,[f] Jean Chang,[c] Lauri Aicher,[c] Katrina M. Waters,[d] Richard D. Smith,[d] Thomas O. Metz,[d] G. Lynn Law,[c] Michael G. Katze,[c,g] Shannon McWeeney,[b] Ralph S. Baric[a,f]

Department of Epidemiology, University of North Carolina at Chapel Hill, Chapel Hill, North Carolina, USA[a]; Division of Bioinformatics and Computational Biology, Department of Medical Informatics and Clinical Epidemiology, Oregon Health Sciences University, Portland, Oregon, USA[b]; Department of Microbiology, School of Medicine, University of Washington, Seattle, Washington, USA[c]; Oregon Clinical and Translational Research Institute, Oregon Health Sciences University, Portland, Oregon, USA[d]; Department of Genetics, University of North Carolina at Chapel Hill, Chapel Hill, North Carolina, USA[e]; Department of Microbiology and Immunology, University of North Carolina at Chapel Hill, Chapel Hill, North Carolina, USA[f]; Washington National Primate Research Center, University of Washington, Seattle, Washington, USA[g]

ABSTRACT **Systems biology offers considerable promise in uncovering novel pathways by which viruses and other microbial pathogens interact with host signaling and expression networks to mediate disease severity. In this study, we have developed an unbiased modeling approach to identify new pathways and network connections mediating acute lung injury, using severe acute respiratory syndrome coronavirus (SARS-CoV) as a model pathogen. We utilized a time course of matched virologic, pathological, and transcriptomic data within a novel methodological framework that can detect pathway enrichment among key highly connected network genes. This unbiased approach produced a high-priority list of 4 genes in one pathway out of over 3,500 genes that were differentially expressed following SARS-CoV infection. With these data, we predicted that the urokinase and other wound repair pathways would regulate lethal versus sublethal disease following SARS-CoV infection in mice. We validated the importance of the urokinase pathway for SARS-CoV disease severity using genetically defined knockout mice, proteomic correlates of pathway activation, and pathological disease severity. The results of these studies demonstrate that a fine balance exists between host coagulation and fibrinolysin pathways regulating pathological disease outcomes, including diffuse alveolar damage and acute lung injury, following infection with highly pathogenic respiratory viruses, such as SARS-CoV.**

IMPORTANCE **Severe acute respiratory syndrome coronavirus (SARS-CoV) emerged in 2002 and 2003, and infected patients developed an atypical pneumonia, acute lung injury (ALI), and acute respiratory distress syndrome (ARDS) leading to pulmonary fibrosis and death. We identified sets of differentially expressed genes that contribute to ALI and ARDS using lethal and sublethal SARS-CoV infection models. Mathematical prioritization of our gene sets identified the urokinase and extracellular matrix remodeling pathways as the most enriched pathways. By infecting Serpine1-knockout mice, we showed that the urokinase pathway had a significant effect on both lung pathology and overall SARS-CoV pathogenesis. These results demonstrate the effective use of unbiased modeling techniques for identification of high-priority host targets that regulate disease outcomes. Similar transcriptional signatures were noted in 1918 and 2009 H1N1 influenza virus-infected mice, suggesting a common, potentially treatable mechanism in development of virus-induced ALI.**

Received 18 April 2013 **Accepted** 9 July 2013 **Published** 6 August 2013

Citation Gralinski LE, Bankhead A, III, Jeng S, Menachery VD, Proll S, Belisle SE, Matzke M, Webb-Robertson B-JM, Luna ML, Shukla AK, Ferris MT, Bolles M, Chang J, Aicher L, Waters KM, Smith RD, Metz TO, Law GL, Katze MG, McWeeney S, Baric RS. 2013. Mechanisms of severe acute respiratory syndrome coronavirus-induced acute lung injury. mBio 4(4):e00271-13. doi:10.1128/mBio.00271-13.

Editor Terence Dermody, Vanderbilt University School of Medicine

Address correspondence to Ralph S. Baric, rbaric@email.unc.edu.

Severe acute respiratory syndrome coronavirus (SARS-CoV) emerged in 2002 and 2003 in China after evolving from related virus species circulating in bats (1, 2). This novel group II coronavirus infected over 8,000 people worldwide, with a mortality rate of ~10% (3). In 2012, a novel human betacoronavirus from group 2c named Middle East respiratory syndrome coronavirus (MERS-CoV) emerged in the Middle East. This virus causes severe pneumonia and renal failure with an approximately 55% mortality in over 77 confirmed cases to date (4). SARS-CoV primarily infected type II pneumocytes, which are normally responsible for production of lung surfactants and function as the progenitor cells of type I pneumocytes (5). Disease severity was heavily influenced by age and other comorbidities, as mortality rates were >50% in populations over 65 years of age.

Acute SARS-CoV infection resulted in denudation of airway epithelial cells, often accompanied by the accumulation of debris, which obstructed airway functions (6, 7). Progression to acute lung injury (ALI) and the more severe form, acute respiratory distress syndrome (ARDS), often involved an acute-phase diffuse alveolar damage (DAD), which is characterized by exudates and hyaline membranes in the lung alveoli (5). Biopsy and autopsy findings from SARS patients within the early stages of infection

revealed the presence of exudative-phase DAD along with increased numbers of macrophages in the lung (1, 6). Many patients also had lung hemorrhage, noncardiogenic pulmonary edema, and/or hyaline membrane formation in the alveolar spaces. Patients with longer-term disease (>10 days postinfection [dpi]) manifested with proliferative- or organizing-phase DAD that encompassed 25% to 100% of the lung (8). They also had signs of lung fibrosis in both alveolar and interstitial spaces. SARS survivors continue to show lingering effects of their illness with complications including reduced lung elasticity and function (9).

ALI and the development of DAD may also occur with other respiratory virus infections, including influenza virus (H5N1 or H1N1-2009) and adult respiratory syncytial virus (RSV) infection, especially in the elderly (10–12). Much like SARS-CoV infection, disease progression is first associated with an exudative phase of DAD, which may progress into organizing-phase DAD (13). The presence of exudates in the lung, composed of fibrin and proteinaceous material, blocks normal gas exchange (14). Without clearance of these exudates, lung pathology progresses toward fibrotic disease with collagen deposition and conversion of the exudates into fibrous tissue. Thus, ALI and ARDS represent a common but poorly studied host response to virus-induced severe lung disease.

Correlation-based gene coexpression network inference approaches are unbiased and powerful tools that can be used to analyze large multidimensional data sets, including expression microarray and proteomics data. Specifically, they capture complex relationships between host gene expression patterns and emergent correlative behaviors (15–17). These approaches posit that genes and protein products are organized into functional modules according to cellular processes and pathways. In this work, we use weighted gene correlation network analysis (WGCNA) methods to interpret the dynamic SARS-CoV-mediated transcriptional response. While WGCNA has previously been applied to cancer, mouse, and yeast genetics, we use the approach to enhance systems-based analysis of virus infection (18–20). Key to this approach is the ability to discover systemic gene expression patterns based on underlying correlation structures, which is not biased by existing knowledge of pathways or interactions. WGCNA partitions gene expression into groups of transcripts called subnetwork modules with highly correlated behaviors. It has been shown elsewhere that connectivity inferred through WGCNA is a strong predictor of related biological function (21). A key feature of these subnetwork modules, or eigengenes, is that the most highly connected hub genes within the module provide candidate mediators of disease (16, 17). We further refined these candidates by modifying the tool to identify enriched pathways associated with candidate lists, allowing us to combine connectivity and predicted network structure with biological functions and known interactions within a hypothesis-testing framework.

Pathogenesis in mouse-adapted-SARS-CoV-infected animals closely mimics the pathologies that were observed in human patients (22), including age-dependent disease severity. To model system-wide behaviors following SARS-CoV infection, we performed a dose-response study that included biological sampling at multiple time points, transcriptional and proteomic systems biology data, and mathematical modeling algorithms to identify signaling networks associated with progression from severe to lethal disease outcomes. These data demonstrate the successful use of highly refined modeling algorithms to identify and validate novel genes and pathways that play critical roles in SARS-CoV pathogenesis and the development of ALI following virus infection in the lung.

In a healthy lung, fibrin levels are controlled through the action of the enzyme plasmin and the urokinase pathway through extracellular matrix (ECM) remodeling (23). ECM remodeling also involves complex interactions between a number of metalloproteinases and their respective regulatory protein networks (24). Disruption of the urokinase pathway is associated with fibrotic lung disease or lung hemorrhage, depending on highly directional signaling cascades. Tissue plasminogen activator (tPA or PLAT), negatively regulated by Serpine1, is given as an anticlotting agent to recent stroke patients to promote cleavage of plasminogen into plasmin and enhance breakdown of fibrin clots (25). Although ECM and wound healing pathway activation are known to be important in lung disease, these processes are largely unstudied in relation to *in vivo* respiratory virus pathogenesis. In this work, we demonstrate a critical role for the urokinase pathway in regulating severe end-stage lung disease outcomes following SARS-CoV infection.

RESULTS

SARS-CoV infection model. To develop an unbiased strategy to explore the molecular mechanisms regulating SARS-CoV pathogenesis and host responses, we studied virus replication kinetics, clinical disease severity, pathological changes, and variations in host transcriptomics along with targeted proteomics using a dose escalation study. The goal was to identify contrasting outcomes for modeling the role of host responses in disease. Groups of 20-week-old C56BL6/J (B6) mice were infected with 10^2 to 10^5 PFU of recombinant mouse-adapted SARS-CoV (MA15) or mock infected (phosphate-buffered saline [PBS]). Clinical changes were noted daily, and biological samples were collected at 0, 1, 2, 4, and 7 days postinfection (dpi) to allow for profiling of the different phases of infection. Mice infected with the lowest dose, 10^2 PFU, lost little if any weight and showed few clinical signs of disease (Fig. 1A). Mice infected with 10^3 or 10^4 PFU experienced transient weight loss and showed minor clinical signs of disease. Infection with 10^5 PFU resulted in continuous weight loss with ≥30% weight loss by day 7; at late time points, these animals showed significant clinical disease, including hunched posture, ruffled fur, decreased locomotion, labored breathing, and death.

Virus load in the lung was quantified by plaque assay and was reflective of both the initial infectious dose and the overall replication kinetics. Mice infected with 10^2 PFU of MA15 had relatively low or undetectable titers (Fig. 1B). Infection with the three higher doses resulted in the highest titers at 1 or 2 dpi, an ~1-log drop in titer at 4 dpi, and a decrease of several logs by 7 dpi, regardless of changes in weight loss. Virus load was confirmed by quantitative PCR (qPCR) for both virus genome and specific viral genes (see Fig. S1A in the supplemental material; also data not shown). Consistent with a previous report (22), minimal to no detectable virus was found in the serum or other organs at 4 dpi (see Fig. S1B to D), and no detectable virus was present in these other organs or serum at day 7.

Pathological findings. Lung pathology varied by both infectious dose and time but was not dependent on virus load. Full histology scoring is available in Table S1A in the supplemental material. At 1 dpi, infected mice showed few inflammatory cells and healthy conducting airways, alveoli, and vasculature. By day 2,

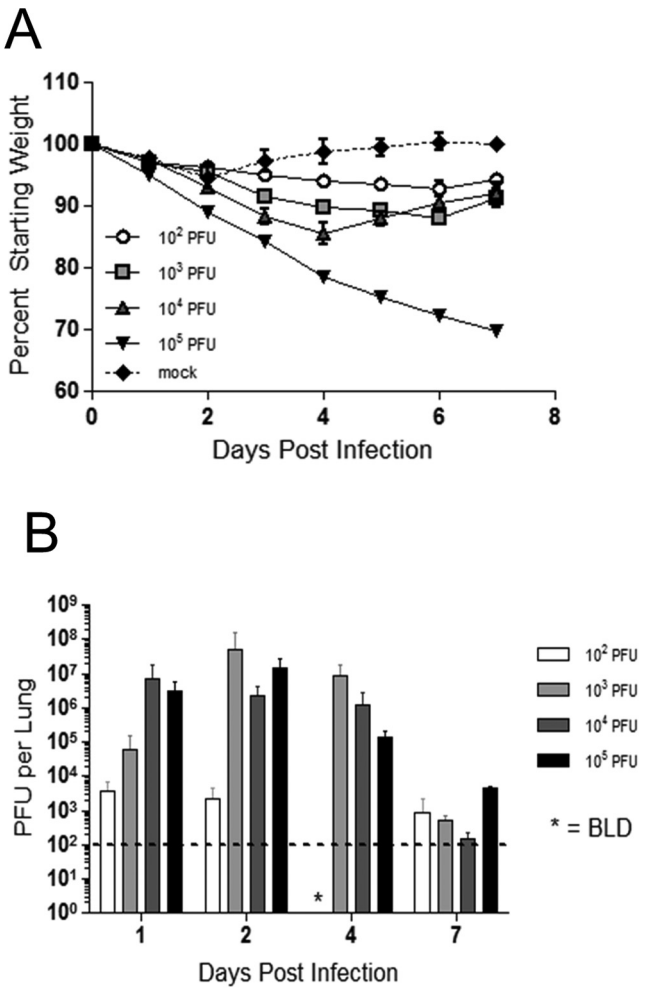

FIG 1 SARS MA15 dose response. (A) Weight loss is shown as percent starting weight over the course of a 7-day infection in 20-week-old B6 mice. Mice infected with 10^2 to 10^4 PFU of SARS-CoV MA15 had low levels of transient weight loss, while mice infected with 10^5 PFU showed increasing weight loss over time. (B) Virus titer in the lung was quantitated by plaque assay. The mean value of all samples with detectable virus in each group is shown (three mice at 10^2 PFU and two each at 10^3, 10^4, and 10^5 PFU had detectable virus by plaque assay at day 7; BLD, below the limit of detection of 100 PFU per lung).

mice in all infection groups showed damage to the large and small conducting airways of the lung in a dose-dependent manner, consisting of denuded patches of airway epithelial layers and apoptotic debris, often obstructing the small airways. At 4 dpi, all infected animals had low levels of epithelial cell denudation and airway debris along with mild thickening of the interstitial membranes. Low-level perivascular cuffing was also present at this time point, and moderate, sporadic hemorrhage was consistently observed in mice infected with 10^3 to 10^5 PFU of MA15 at 4 dpi.

By 7 dpi, lung disease was most pronounced in the parenchyma in mice infected with a 10^5-PFU dose and included thickening of the interstitial septum, inflammatory infiltrates including neutrophils, and pink proteinaceous exudates, typical of DAD (see Fig. S1E in the supplemental material). Importantly, these mice had clearly visible hyaline membranes, a characteristic of fatal SARS-CoV infection in humans (26). These mice also showed severe and complete lung hemorrhage at 7 dpi, while mice infected with 10^4 PFU had moderate but notable hemorrhage (see Table S1A). Mice infected with lower doses had only mild to moderate vascular cuffing and interstitial inflammation along with sporadic and mild hemorrhage but were otherwise absent of severe lung disease.

Global host expression patterns. Lung gene expression patterns were compared between mice with each infection dose and mock-infected mice to gain insight into SARS-CoV-induced lung disease. Consistent with earlier reports (27), there was minimal differential expression (DE) at the transcript level at 1 dpi (i.e., $|\log_2$ fold change [FC]$|$ of >1.5 and false discovery rate [FDR] adjusted P value of <0.05), regardless of infectious dose (Fig. 2A). However, the number of DE genes escalated with increasing dose or number of days postinfection. Overlap of DE genes was determined between mice infected with 10^4 PFU and those infected with 10^5 PFU. The maximum percentage of overlap in DE genes was measured at 1 and 2 dpi, despite the low number of DE genes. The least overlap between these doses was measured at 7 dpi (Fig. 2B), with 23% of genes showing DE at 10^5 PFU but not at 10^4 PFU. We hypothesized that these genes with different expression patterns in mice infected with 10^5 PFU (here referred to as the lethal dose) from those in mice infected with 10^4 PFU (here referred to as the sublethal dose) could provide insight into the molecular mechanisms and host expression patterns that regulate lethal versus sublethal disease following SARS-CoV infection.

Eigengene network analyses following SARS-CoV infection. Gene expression patterns were compared between mice infected with the sublethal dose and lethal dose using the WGCNA approach (28). In the consensus network analysis, 24 module eigengenes (clusters of genes with similar expression patterns over time) were identified (23 with statistically significant connectivity; P value of <0.0001 using permutation test) (Fig. 3A). Many of the eigengenes represented groups of genes with similar expression patterns and dynamics between the lethal and sublethal doses. We chose to focus on one specific module eigengene that displayed distinct dose dynamics, hypothesizing that the differences in transcript expression could explain the differential disease outcome.

The eigengene that we pursued, shown in blue and circled in Fig. 3A, had significantly higher expression at 2, 4, and 7 dpi in lethally infected mice than in sublethally infected mice (Fig. 3B; expression patterns for the other statistically significant eigengenes can be found in Fig. S2 in the supplemental material). This module was prioritizing based on differential expression between doses at day 7 based on overall upregulation in the lethal dose infection and differential module regulation when comparing doses. Specifically, Δ average $\log_2$ fold change (FC) was calculated by subtracting the average $\log_2$ FC for each dose. Using this strategy, we selected the blue module because it is strongly upregulated for the lethal dose (1.28 average $\log_2$ FC) while the sublethal dosing was only mildly upregulated (0.36 average $\log_2$ FC) and the resulting Δ average $\log_2$ FC was 0.93 (an almost 2-fold difference). This eigengene module was comprised of 760 differentially expressed transcripts.

When the unbiased gene list from the blue module was analyzed by the GeneGo Metacore knowledge base, the top functional categories were related to cell adhesion, ECM remodeling, and wound healing (see Table S2 in the supplemental material). The same knowledge base was used to visualize the highest-priority ECM remodeling signaling pathways containing proteins en-

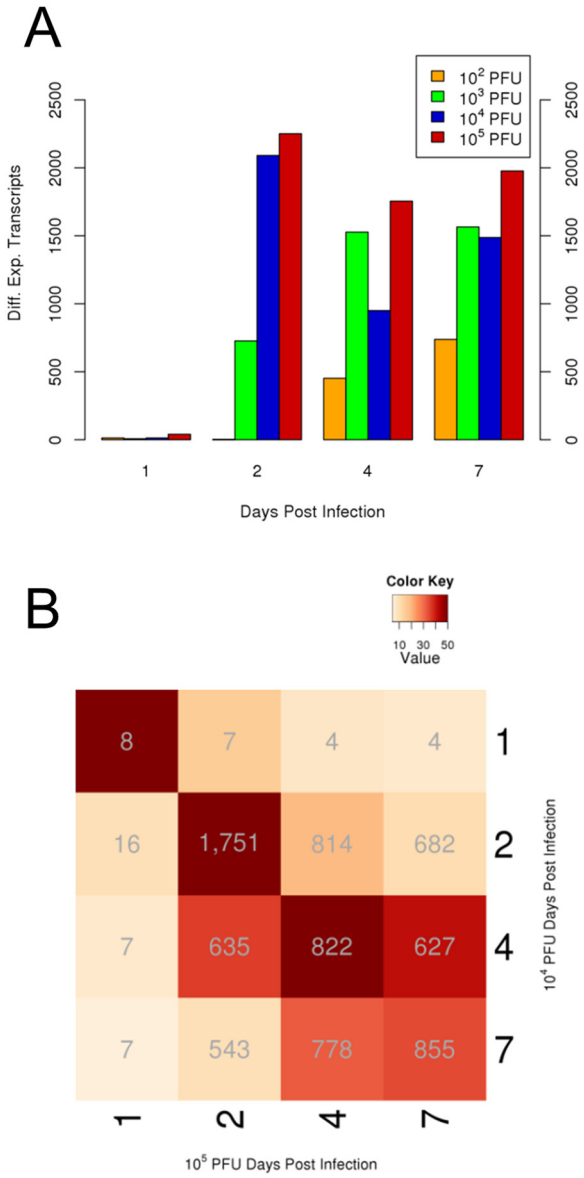

FIG 2 Dose-response differential gene expression. (A) Differential expression (DE) of transcripts for each dose is shown at each day postinfection. The number of DE transcripts was greatest for sublethal (10^4-PFU) and lethal (10^5-PFU) infections at day 2, with 2,091 and 2,251, respectively. In total across all 4 days, there were 3,138 unique DE transcripts for the 10^4-PFU infections and 3,683 for the 10^5-PFU infections. (B) The heat map shows the number of overlapping transcripts for each time point in both sublethal- and lethal-dose MA15 infections. Coloring represents the odds ratio or the effect size of each overlap, and gray numbers within the cells are the numbers of common differentially expressed (DE) transcripts. Analogous to differences in phenotype between infection doses, the overlap is strongest at day 2 and weakest at day 7 postinfection.

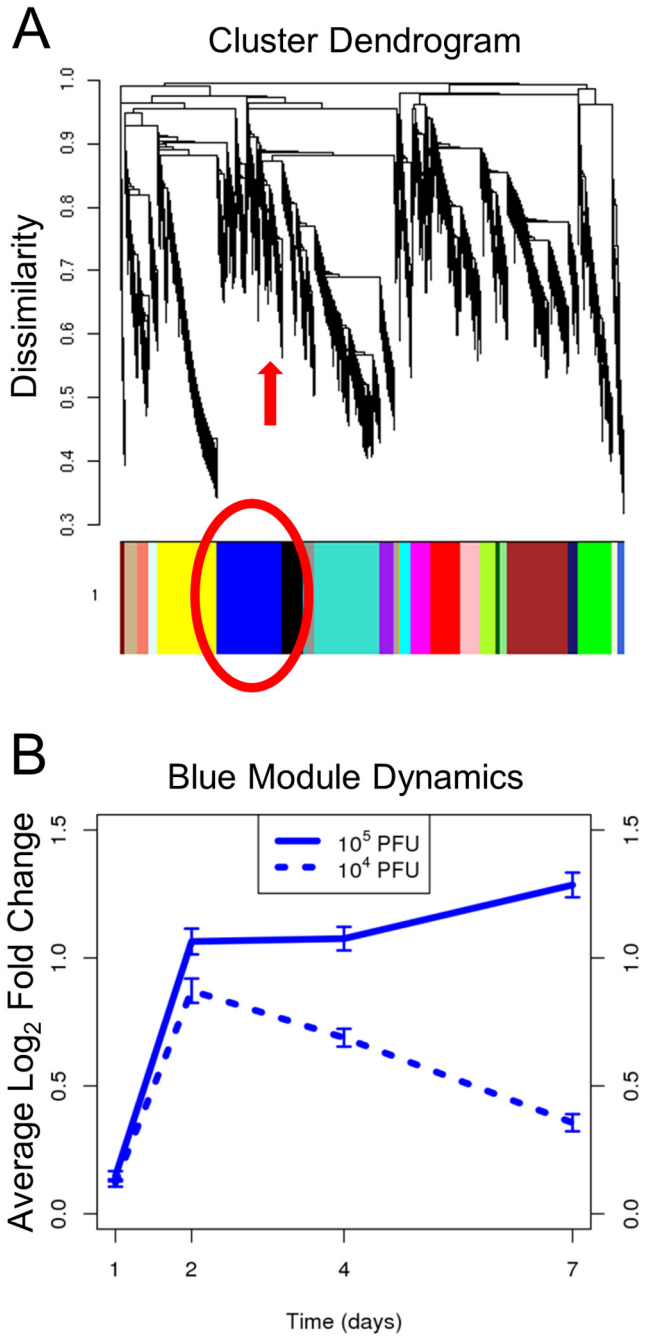

FIG 3 Eigengene analysis. The consensus network is represented as a dendrogram (A), and modules are shown as colors below. The blue module (circled in red) displayed distinct behavior for each dose (10^4 and 10^5 PFU), indicating potential mediators of MA15 infection pathogenesis (B). The arrow in panel A indicates the approximate location of *Serpine1* and *PLAT* within the blue module.

coded by the gene set with differential signaling in lethally or sublethally infected mice (see Fig. S3). To further refine our candidates, we assessed the connectivity and module membership within known biological pathways. The full statistical analysis workflow is described in Materials and Methods, and a diagram of the workflow is shown in Fig. S4. The urokinase pathway was the most significantly enriched for both module membership (*P* value = 0.000793, odds ratio [OR] = 8.31) and transcriptional connectivity (*P* value = 0.0126, 10,000 permutations), making it the ideal target for validation. While the eigengenes themselves were not priority ranked, the unbiased method that we used to prioritize targets within the blue eigengene model could easily be applied to other modules.

The urokinase pathway contributes to the broader ECM remodeling pathway shown in Fig. S3 in the supplemental material,

and its members, including *Serpine1*, *Serpine2*, *PLAT*, and *PLAUR*, along with other ECM remodeling genes, show significantly higher expression at 7 dpi in the lethal dose than in the sublethal dose (see Fig. S5A). While the urokinase pathway has not previously been associated with respiratory virus infection, its involvement in ischemic events and metastatic cancers has been well documented (29). Furthermore, fibrin turnover and alveolar coagulopathy are known to significantly contribute to the severity of ALI following injury or chemical insult (30). Based on these factors, we explored the impact of the urokinase pathway on SARS-CoV infection.

Acute lung injury following acute severe respiratory infection. Expanding on the identification of the urokinase pathway, we examined whether conserved RNA expression signatures indicated development of a procoagulant or profibrinolytic state after SARS-CoV infection. Tissue factor, factor VIIa, and Serpine1 are major factors responsible for the development of a procoagulant and antifibrinolytic state in the alveoli (31, 32). Changes in alveolar hemostatic balance and intra-alveolar fibrin deposition are also stimulated by cytokine expression after ALI. Proinflammatory (interleukin-1β [*IL-1*β], tumor necrosis factor alpha [*TNF-*α], and *IL-6*) and profibrotic (transforming growth factor β [*TGF-*β], connective tissue growth factor [*CTGF*], and platelet-derived growth factor [*PDGF*]) cytokine transcripts were significantly elevated, starting by 4 dpi and through the course of the lethal SARS-CoV MA15 infection (see Fig. S5B in the supplemental material). In addition, genes associated with the induction of a procoagulant state (*thrombin*, *factor VIIa*, *factor Xia*, *factor XIIa*, *PLAU*, *PLAT*, *tissue factor F2r*) (32) and other fibrinolysin pathway components were altered by infection. Both pro- and antifibrinolytic genes in the urokinase pathway showed increased expression in our SARS-CoV infection model, demonstrating the complicated nature of this signaling cascade. Previous reports show that it is rare for one branch of the urokinase pathway to have altered regulation without host feedback loops adjusting the expression of other pathway genes (33). In general, the transcripts shown in Fig. S5B represent a lung with high levels of inflammatory and fibrinolytic gene expression, and this transcriptional picture is supported by the hemorrhage observed in the lungs of SARS-CoV-infected mice.

To increase our understanding of the changes in the lung following acute viral infection, we examined microarray data from previously published respiratory infection models of ARDS. Transcriptional data from the lungs of 1918 influenza virus-infected BALB/c mice showed similar patterns of differential expression in the genes responsible for coagulation, surfactant production, and fibrinolysis (see Fig. S6 in the supplemental material). Furthermore, B6 mice infected with the 2009 H1N1 influenza virus strain CA04 had high levels of proinflammatory, profibrotic, and urokinase pathway gene expression relative to mock-infected mice along with decreased surfactant expression (doses of 10^3 to 10^6 PFU [unpublished data]). Overall, these transcription signatures are consistent with reported viral pathological and proteomic findings, strongly supporting the development of altered alveolar hemostatic balance seen during the early exudative phase of DAD.

Urokinase pathway in SARS-CoV pathogenesis. To further investigate the role of the urokinase and ECM remodeling pathways, we analyzed lung proteomics. Proteomics analysis revealed that fibrin beta and gamma chains, factor VIII, and cytokeratins, all major components of hyaline membranes (34, 35), have increased expression in the lungs following both lethal and sublethal SARS-CoV infection compared to mock infection (Fig. 4A). Similarly, surfactant proteins, which typically protect against hyaline membrane formation and lung injury (36), have reduced expression in both the lethal and sublethal doses of SARS-CoV compared to uninfected controls. However, at late time points, several of these same proteins sharply diverge between the lethal and sublethal doses. Fibrin beta and gamma chain levels are increased in abundance relative to mock infection only at day 7 in the lethal infection. In contrast, fibrin chains continually decrease after 2 dpi in sublethal infection. A similar pattern is observed with keratin 7, with increased protein abundance observed in the lethal dose. To further confirm these findings, we used a Martius scarlet blue (MSB) stain to demonstrate the presence of fibrin deposition in the lungs at day 7. Positive staining was observed in the lungs of lethally infected mice but not in the lungs of mock-infected or sublethally infected animals (Fig. 4B). Together, the proteomics data are consistent with pathophysiological changes resulting in increased fibrin deposition and hyaline membrane formation in the lungs of lethally infected mice.

Fibrin is cleaved and degraded by plasmin, having been converted from plasminogen by urokinase pathway members (23). Analysis of plasminogen peptides revealed a distinct and significant increase following a lethal dose of SARS-CoV (Fig. 4A). In contrast, the sublethal infection resulted in an initial augmentation but then maintained a low level of plasminogen peptides throughout the course of infection. It is important to note that plasminogen and plasmin are indistinguishable using these proteomics methods. Fibronectin, another component downstream of plasmin activation, also demonstrated increased protein expression in the lethal dose compared to the sublethal dose at day 7. These data are consistent with augmented PLAU/urokinase activity in the lethal dose despite maintaining similarly elevated levels of Serpine1, an inhibitor of the urokinase pathway. Finally, diseases associated with premature or excessive breakdown of fibrin clots are characterized by hemorrhage and the accumulation of fluid exudates in the alveoli. Consistent with the observation of vascular leakage into alveolar spaces and the development of DAD, levels of the serum protein albumin found in the lung were significantly elevated in lethally infected mice (Fig. 4A).

Targeted knockout mice. To complete the systems biology loop (broad study, model/hypothesis generation, and then testing of the model), we selected a targeted member of the urokinase pathway for validation studies. Genes within the blue module were ranked according to their overall connectivity and agreement with the module eigengene expression, and *Serpine1* was the highest-ranked urokinase pathway member (correlation with the module eigengene [K_{me}] of 0.859). The approximate location of *Serpine1* within the blue module is highlighted in Fig. 3A. Serpine1$^{-/-}$ mice infected with a sublethal dose of MA15 continued to lose weight through day 7 postinfection (Fig. 5A) and showed significantly more weight loss than did B6 controls at days 5 to 7 postinfection (P value of <0.05). Additionally, one Serpine1$^{-/-}$ mouse died, suggesting a necessary and protective role for Serpine1 in modulating SARS-CoV pathogenesis. Clinical disease in Serpine1$^{-/-}$ mice mirrored that in lethally infected B6 animals (Fig. 1A), with severely decreased locomotion, hunched posture, and labored breathing at late time points. Despite differences in clinical symptoms, virus load in the lung showed no significant

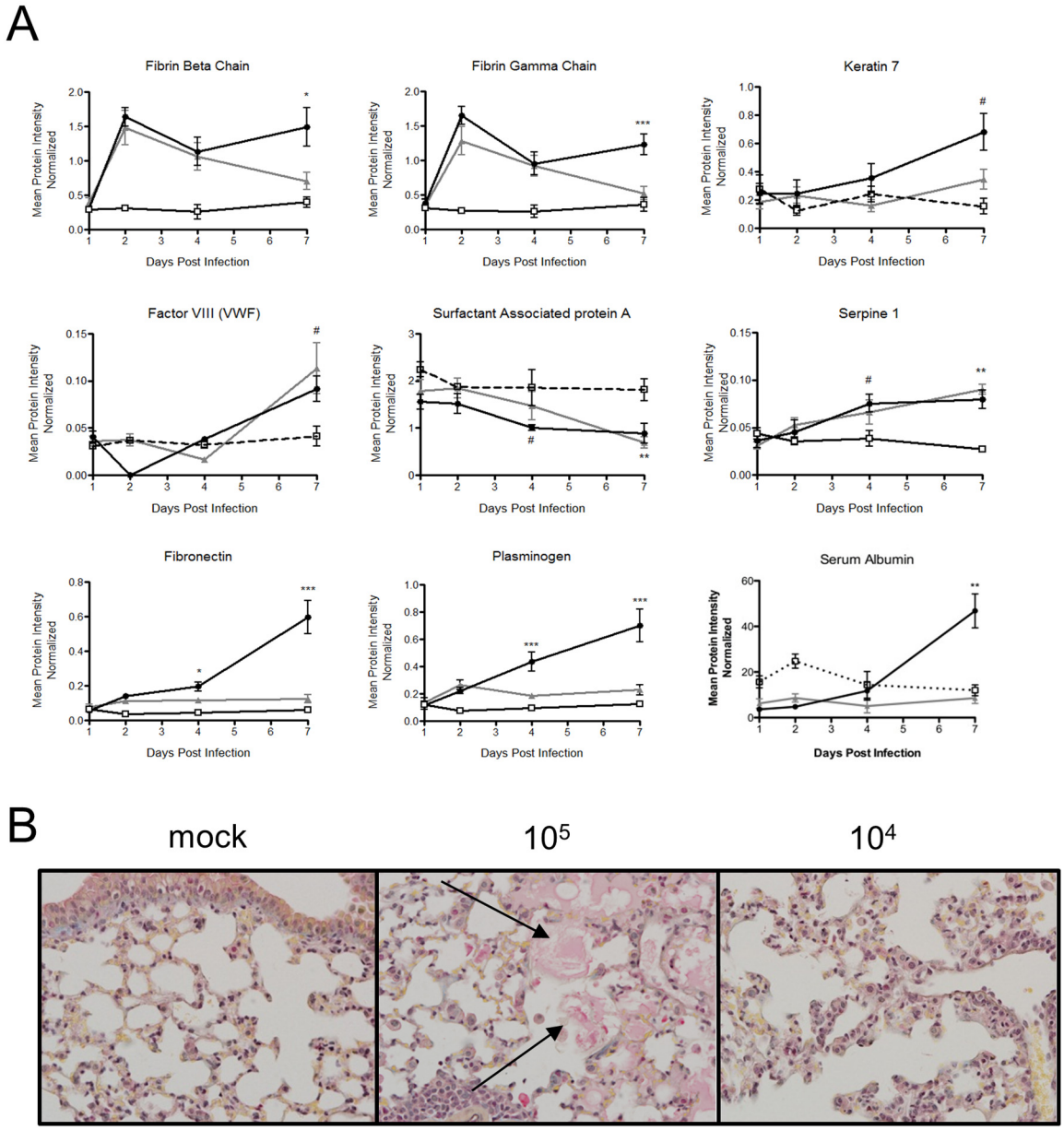

FIG 4 (A) Identification of urokinase and tissue remodeling pathway members. (A) Peptide levels from total lung homogenates were analyzed to determine expression of select ECM and urokinase pathway proteins. Mock-infection values are shown by dashed lines, sublethal infection values are shown by gray lines, and lethal infection values are shown by black lines. Significance values: *, $P < 0.05$; **, $P < 0.01$; ***, $P < 0.001$; #, lethal dose significant at $P < 0.05$. VWF, von Willebrand factor. (B) Lung sections from 7-dpi lethally or sublethally infected mice or mock-infected mice were stained for the presence of fibrin using MSB (Martius scarlet blue). Yellow staining indicates red blood cells, blue staining indicates connective tissue, and red staining indicates fibrin. Arrows point to positive fibrin staining.

differences between knockout and wild-type (WT) mice (Fig. 5B) at 4 or 7 dpi, demonstrating that Serpine1 had no influence on virus replication dynamics. When B6 and Serpine1$^{-/-}$ mice were infected with the lethal dose of SARS-CoV, the Serpine1$^{-/-}$ mice succumbed to infection sooner than did the B6 controls (Fig. 5C) (P value of <0.01), further indicating a protective role for Serpine1 and the urokinase pathway in SARS-CoV-induced disease. While 10^5 PFU is lethal in 20-week-old B6 mice, wild-type mice rarely succumb before 7 dpi.

Examining lung sections, we observed cuffing of inflammatory cells around the large airways and vasculature of all infected mice at 4 dpi (see Table S1B in the supplemental material), which increased by 7 dpi. At 4 dpi, there was mild interstitial membrane thickening and low numbers of inflammatory cells were observed in the alveolar spaces of all infected mice; by 7 dpi, disease in the parenchyma had developed to moderate levels. Gross hemorrhage levels of the lung were noted at the time of tissue harvest. Serpine1$^{-/-}$ mice trended toward increased hemorrhage in their lung tissue compared to B6 controls at day 4, and by 7 dpi, the knockout mice exhibited significantly more lung hemorrhage

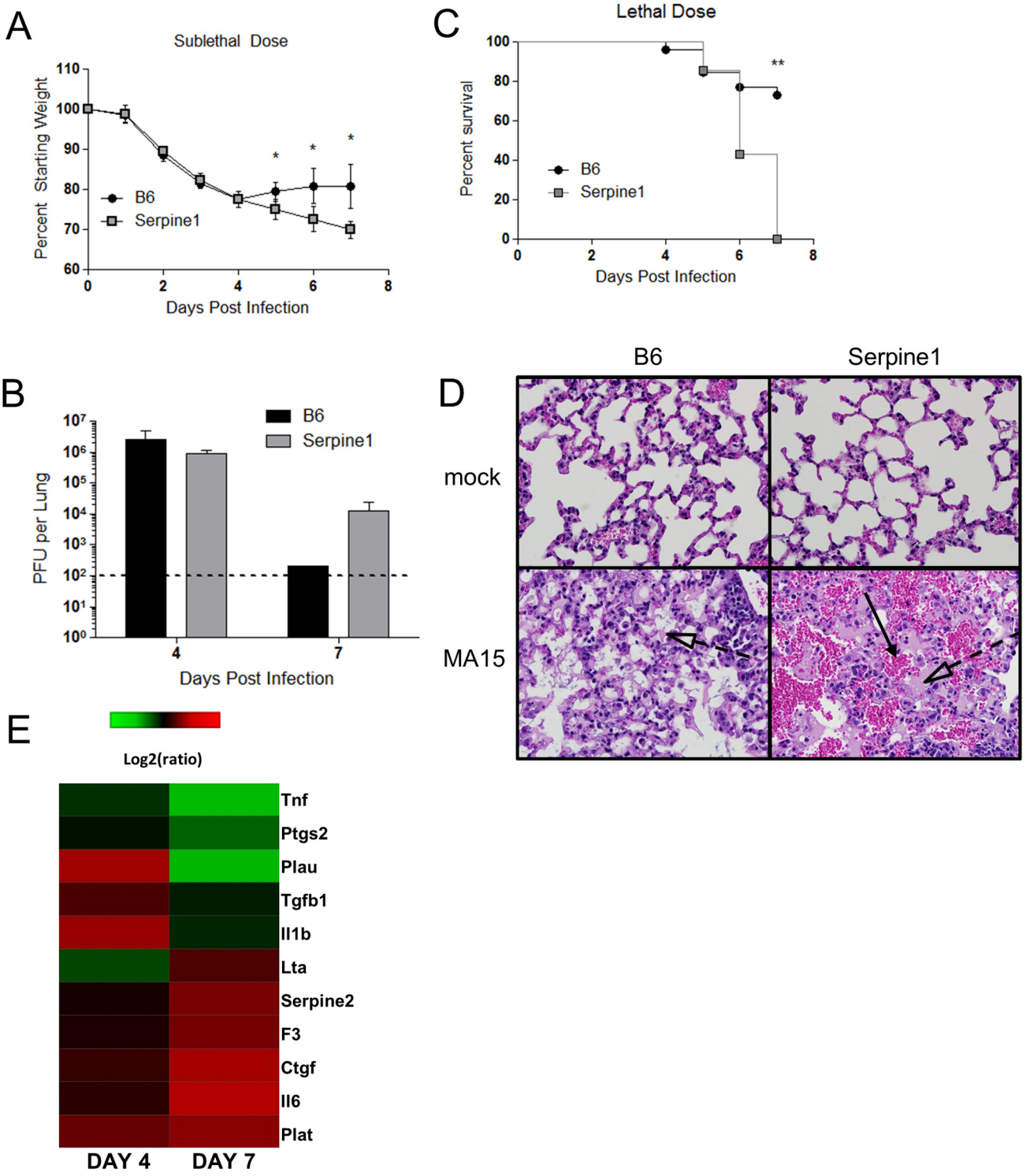

FIG 5 Serpine1$^{-/-}$ mice are susceptible to SARS-CoV infection. (A) Serpine1$^{-/-}$ mice lost more weight than did B6 control mice when infected with 10^4 PFU of SARS-CoV MA15 (P value of <0.05 for Serpine1 versus B6 at days 5, 6, and 7 postinfection). (B) Serpine1$^{-/-}$ mice succumbed to infection more rapidly than did B6 controls when infected with 10^5 PFU of MA15 (** = P value of <0.01). (C) Lung mean virus load was quantitated by plaque assay. There was no statistical difference in viral titers at 4 dpi; at 7 dpi, most mice had lung titers below the limit of detection (BLD, <100 PFU; two Serpine1$^{-/-}$ mice and one B6 control mouse with detectable virus). Independent replicate experiments confirmed significant differences in weight loss but no difference in lung titer between Serpine1$^{-/-}$ and B6 controls at both 4 and 7 dpi (data not shown). (D) Representative histology images from Serpine1$^{-/-}$ or B6 mouse lungs at 7 days postinfection show that infected knockout mice had extensive hemorrhage after infection with MA15. Exudates are indicated by open arrows with dashed lines; hemorrhage is shown by filled arrows with solid lines. (E) Log_2 fold change ratio of ARDS-related gene expression from the lungs of SARS-CoV-infected Serpine1$^{-/-}$ and B6 mice at 4 and 7 dpi (log_2 fold change = mean log_2 FC [WT] − mean log_2 FC [knockout]). Green indicates that expression in Serpine1-knockout mice is lower than that in B6 mice, and red indicates that expression in Serpine1-knockout mice is higher than that in B6 mice.

(P value of <0.05 by Student's t test) (Fig. 5D). Combined, these data confirm our model prediction that Serpine1 and the urokinase pathway play an important role in the pathogenesis of SARS-CoV infection.

Examination of gene expression in the lungs of Serpine1$^{-/-}$ mice and B6 controls showed that SARS infection causes greater *PLAT*, *IL-6*, tissue factor (*F3*), and *Serpine2* expression in the absence of Serpine1 (Fig. 5E). Serpine2 functions similarly to Serpine1 in control of PLAT and PLAU activity. *IL-1β*, *Tgfb1*, and *PLAU* all had increased expression in Serpine1$^{-/-}$ lungs at day 4 relative to B6 controls but decreased expression at day 7, while *Ptgs2* and *Tnf* had decreased expression in the Serpine1$^{-/-}$ mice at both time points. These data support the existing evidence of feedback loops within the urokinase pathway as well as confirming the overall dysregulation of the urokinase pathway following SARS-CoV infection. Combined, these transcriptional changes indicate that SARS-CoV-infected Serpine1$^{-/-}$ mice had increased fibrinolytic activity in their lungs and a decreased inflammatory response relative to B6 controls. A simplified schematic of the urokinase pathway in the presence and absence of Serpine1 is shown in Fig. 6A and B, illustrating how the lack of Serpine1 could lead to increased PLAT and PLAU activity and increased hemorrhage and disease.

To further confirm the importance of the urokinase pathway in SARS-CoV pathogenesis, we infected mice deficient in PLAT, one of the two plasmin-cleaving proteins that are activated by Serpine1. *PLAT* expression was also highly connected to that of the overall blue module with a K_{me} of 0.815. Mice deficient in PLAT should have a complicated phenotype because of the ability of PLAU to cleave fibrin and compensate in this system. Sublethally infected PLAT$^{-/-}$ mice showed a slight, but not statistically significant ($P = 0.06$), acceleration in recovery of weight loss compared to B6 controls (see Fig. S7A in the supplemental material) and a significant increase in exudates in the lung ($P < 0.05$; see Fig. S7E). In contrast, PLAT$^{-/-}$ mice infected with a lethal dose of MA15 showed notable early mortality compared to B6 controls, although those knockout mice that survived early infection went on to recover (see Fig. S7B and C). Lethally infected PLAT$^{-/-}$ mice also trended toward less hemorrhage in their lungs than did B6 controls. B6 and PLAT mice infected with equal doses of MA15 had similar virus loads in the lung at both 4 and 7 days postinfection (see Fig. S7D), demonstrating that manipulation of the urokinase pathway did not influence virus replication dynamics but instead impacted the host response in regulating the development and resolution of ALI.

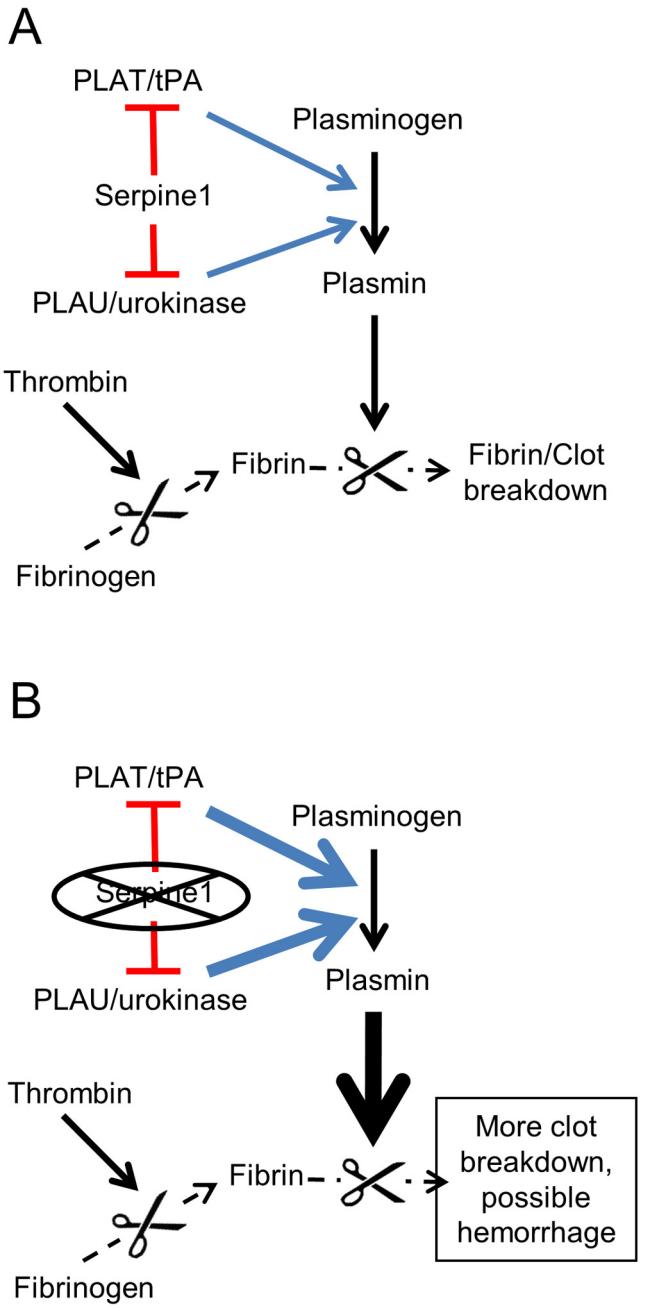

FIG 6 Urokinase pathway model. (A) Representation of the unperturbed urokinase pathway signaling pathway. (B) Without the presence of Serpine1, an inhibitor of both PLAU/urokinase and PLAT/tPA, there is increased cleavage of plasminogen into the active plasmin and thus increased breakdown of fibrin clots and hemorrhage compared to an unperturbed system. Red T shapes indicate inhibition, and blue arrows indicate activation.

DISCUSSION

In this study, we highlight an unbiased modeling approach using systems biology to investigate viral pathogenesis and identify a novel host pathway involved in SARS-CoV disease progression. While wound healing and extracellular matrix remodeling pathways have previously been associated with lung disease (32), this association had not extended into studies of acute respiratory virus infection. Our data suggest that dysregulation of the urokinase pathway during SARS-CoV infection contributes to more severe lung pathology and that Serpine1 plays a protective role following infection. Similar changes in the urokinase, coagulation, and fibrinolysin pathway expression signatures are noted following highly pathogenic SARS-CoV and influenza virus infections (see Fig. S5B and S6 in the supplemental material), arguing for a conserved role for these pathways in virus-induced end-stage lung diseases, like ALI and ARDS.

The lack of well-defined statistical methods for organizing complex data sets into prioritized modules has hampered the power for systems-based discovery. While gene coexpression networks provide one approach to capture the complex relationships between transcripts, the approach can also be integrated with other types of quantitative data, like infection outcomes, patho-

logical findings, and clinical disease severity, resulting in a clearer distinction between principal components (eigengenes) and biological processes. An important goal of these types of integrative analyses is the deconstruction of large data sets into high-priority, constructive gene signatures that provide predictive power for downstream analysis and validation. However, these types of analyses have rarely moved beyond simulations produced from existing data sets.

We have modified a WGCNA approach to cluster similarly regulated genes into eigengene modules in order to compare and contrast module behavior as a function of virus dose and disease severity. We then developed strategies to prioritize targets for downstream analyses at the level of larger pathway analyses which were followed by analysis of specific genes. This approach was applied to our virus infection data sets containing over 3,500 DE genes. It resulted in the identification and characterization of four highly prioritized genes in the urokinase pathway whose differential expression was significantly associated with increased disease severity. We note that there are a number of enrichment approaches, such as gene set enrichment analysis (GSEA) (37), or hypergeometric test-based approaches, such as GOStat (38), which can identify genes behaving in coordinated ways to aid in interpreting gene candidates. However, these approaches are often focused on differential expression in the context of functional annotation. With our approach, we focus on *de novo*-inferred connectivity and the distribution of the most highly connected module members within canonical pathways. This allows for a much more focused refinement of the candidate list and enables the generation of direct hypotheses for perturbation testing among the candidates.

Our unbiased transcriptomics analysis approach identified 24 eigengenes with different expression patterns (Fig. 3A). The eigengene network analysis and prioritization also identified several highly ranked innate immune signaling components, including *MyD88*, *STAT1*, and *Ptgs2*, as having high connectivity with the severity of SARS-CoV disease outcome. Earlier studies have independently demonstrated that MyD88- and STAT1-knockout mice are highly susceptible to SARS-CoV pathogenesis and that blocking prostaglandin function protects old mice from SARS-CoV pathogenesis (39–41). STAT1 signaling is known to affect cell cycle and apoptotic processes, and STAT1-knockout mice are particularly sensitive to bleomycin-induced lung fibrosis with increased collagen levels and enhanced fibroblast proliferation (42). Together, these previous reports further confirm the efficacy of our modeling approach.

To further validate our model, we analyzed genes from one module eigengene with connections to wound healing and ECM remodeling pathways, including the urokinase pathway, which displayed dose-dependent expression changes. Both histology and proteomic data demonstrated that urokinase activity increased in a dose-dependent manner following SARS-CoV infection. To complete a validation loop, we characterized disease outcomes in Serpine1$^{-/-}$ and PLAT$^{-/-}$ mice. The Serpine1$^{-/-}$ mice, deficient in a major protein in the urokinase pathway, were significantly more susceptible to SARS-CoV infection than were WT controls in terms of both weight loss and lung hemorrhage (Fig. 5A and D), while the PLAT$^{-/-}$ mice showed a mixed pathogenic phenotype that suggested improved outcome but significant impairment of lung function (see Fig. S7A and E in the supplemental material). These data confirm predictions that the urokinase pathway and ECM remodeling are important for regulating SARS-CoV pathogenic outcomes and demonstrate the delicate balance between development of hemorrhage and fibrosis following ALI. While previous studies of SARS-CoV pathogenesis showed the presence of fibrin in the lung following infection, the importance of Serpine1 and the urokinase pathway in development of disease was unknown. Furthermore, the use of unbiased methods to identify the urokinase pathway as a regulator of SARS-CoV disease represents an important advance in analysis of microarray data.

ALI and its more severe form, ARDS, are devastating end-stage lung diseases that can arise following a variety of acute insults to the lung epithelium and occur frequently following infection with SARS-CoV and H5N1 and H1N1 influenza viruses in humans (11, 43, 44). Despite significant advances in treatment options, the overall mortality rates remain substantial and range between 30 and 60%, resulting in ~75,000 deaths in the United States and over a million deaths globally each year (45). While the underlying molecular mechanisms governing virus-induced ALI remain to be elucidated, our transcriptomics, proteomics, modeling, and validation approaches using targeted knockout mice have coalesced into a model of altered hemostatic balance defined by the expression of procoagulative and antifibrinolytic factors resulting in the induction of an exudative phase of DAD after infection. The urokinase pathway regulates fibrinolytic and procoagulative responses designed to prevent vascular permeability and hemorrhage (23, 29).

Fibrin levels dramatically increased following lethal SARS-CoV MA15 infection (Fig. 4A and B). Excess fibrin was likely mediated by Serpine1-driven inhibition of urokinase and tissue type plasminogen activators (PLAU and PLAT) and by blockade of plasmin activity by α2-plasmin inhibitor, whose transcripts are elevated following SARS-CoV infection. We suggest that lethal SARS-CoV infection overwhelms the normally protective, profibrinolytic signaling of the urokinase pathway, leading to overall dysregulation, including increased *Serpine1* expression, and severe lung disease. While fibrin is required for normal wound healing, persistent and excessive intra-alveolar fibrin levels can contribute to acute inflammatory and chronic interstitial lung disease. Fibrin stimulates the production of profibrotic growth factors (32), and many profibrotic cytokine transcripts, like *TGF-β*, *CTGF*, and *PDGF*, are elevated following SARS-CoV or influenza virus infection in mice (see Fig. S5 and S6 in the supplemental material) (46, 47). Pulmonary surfactant protein and transcript signatures are also reduced following acute viral infection (Fig. 4A) (see also Fig. S5) (48), potentially leading to collapse or closure of alveoli and loss of lung compliance (changes in lung volumes) (49). In combination, a high-fibrin/low-surfactant intra-alveolar environment provides an ideal environment for fibroblast adherence and growth, resulting in collagen deposition and development of lung fibrosis (50). Finally, fibrin and fibrin breakdown products increase vascular permeability, stimulate migration and proliferation of inflammatory cells, and promote recruitment of neutrophils to the lung (51, 52). Although we cannot absolutely ascribe this phenotype to elevation in the levels of fibrin and fibrin breakdown products, fluorescence-activated cell sorting (FACS) analysis shows significant increases in lung neutrophil counts, as a function of increasing SARS-CoV dose (data not shown). More recent studies have also shown that Serpine1 inhibits neutrophil apoptosis (53), suggesting that neutrophil recruitment and effector function likely contribute to more severe disease outcomes following SARS-CoV MA15 infection. Similar

findings have been reported with highly pathogenic influenza viruses, including H5N1 and 1918 influenza viruses (54).

Fibrin accumulation in the lung is a hallmark of ALI and ARDS, and a reduced capacity to cleave and remove fibrin deposits corresponds with a poor clinical patient outcome (31). Notably, increased Serpine1 levels were measured in the blood of SARS-CoV-infected patients during the 2002-2003 epidemic, and increased Serpine1 expression has been measured in the lungs of SARS-CoV-infected macaques (55, 56). Necropsy findings from H5N1 influenza patients revealed accumulations of fibrin in the lung along with pulmonary edema and other signs of DAD and hemorrhage (57). Furthermore, 1918 and 2009 H1N1 influenza virus-infected mice showed increased levels of urokinase pathway transcripts (see Fig. S6 in the supplemental material; also data not shown). The host response to *Streptococcus pneumoniae* also includes upregulation of *Serpine1* expression to protect against hemorrhage and ALI. The deubiquitinase CYLD provides critical control of *Serpine1* expression (58), and in the absence of CYLD, infected mice develop lung fibrosis. Experiments using the mouse model for pneumonic plague have shown that deletion of the bacterial plasminogen activator, which cleaves plasminogen and also Serpine1, changes the course of disease and protects mice from lethal lung injury (59). Combined, these data demonstrate the critical balance of coagulative and fibrinolytic signaling in the lung following injury and suggest a common modality for development of pathogen-induced ALI and ARDS after microbial infection.

The systems biology approach promises to aid in our understanding of complex biological processes through the high-throughput, unbiased analysis of broad data sets. Previous work has demonstrated the ability to identify distinct transcriptomic signatures predictive of the immune response to the yellow fever and influenza vaccines (60, 61). Our approach highlights the ability to maintain statistical rigor and analytical prioritization that is both driven by and focused on biological relevance and experimental validation. Using this approach, mathematical models and their predictions, as well as the subsequent perturbations and refinement, allowed us to characterize the molecular mechanisms that lead to the initiation and progression of infectious disease pathogenesis. A comparative approach with multiple viruses, such as SARS virus and highly pathogenic influenza virus, can identify common pathways that lead to severe end-stage lung disease and provide high-value targets for therapeutic approaches that address multiple pathogens. These data demonstrate the successful use of systems biology approaches to identify and then validate novel genes and pathways that play critical roles in SARS-CoV pathogenesis in the lung and suggest targeting urokinase and coagulopathy-related signaling pathways as a therapeutic approach to treat virus-induced ALI.

MATERIALS AND METHODS

Viruses and cells. Recombinant mouse-adapted SARS-CoV (MA15) was propagated on Vero E6 cells, and its titer was determined. For virus titration, half of the right lung was used to give PFU per lung using Vero E6 cells with a detection limit of 100 PFU (62). All experiments were performed in a class II biological safety cabinet in a certified biosafety level 3 laboratory containing redundant exhaust fans by workers wearing personnel protective equipment, including Tyvek suits, hoods, and high-efficiency particulate air (HEPA)-filtered powered air-purifying respirators (PAPRs).

Animals. C57BL/6J (stock no. 000664), Serpine1$^{-/-}$ (stock no. 002507), and PLAT$^{-/-}$ (stock no. 002508) mice were obtained from the Jackson Laboratory (Bar Harbor, ME). Mice were anesthetized with a mixture of ketamine and xylazine and intranasally infected with either 50 μl of phosphate-buffered saline (PBS) alone or MA15 (e.g., 10^2 to 10^5 PFU /animal). Animals were maintained in HEPA-filtered Sealsafe cages (Techniplast, Buguggiate, Italy). All animal housing and care were conducted in accordance with all University of North Carolina (UNC)-Chapel Hill Institutional Animal Care and Use Committee guidelines. Lung tissues from a total of 5 infected mice were harvested at each dose on days 1, 2, 4, and 7 postinfection in the dose-response study. Lung tissues from a total of 4 infected mice were harvested at days 4 and 7 postinfection in the knockout mouse studies. Mock-infected animals were age matched and harvested at each time point. Weight loss significance was determined by Student's *t* test (Microsoft Excel), and significance in survival data was determined by the Mantel-Cox test (GraphPad). qPCR assays were used to confirm the infection status of all mice. All mouse studies were performed at the University of North Carolina (Animal Welfare Assurance #A3410-01) using protocols approved by the UNC Institutional Animal Care and Use Committee (IACUC).

Histological analysis and hemorrhage. Gross hemorrhage of lung tissue was observed immediately after euthanasia and scored on a scale of 0 (no hemorrhage in any lobe) to 4 (extreme and complete hemorrhage in all lobes of the lung). Lung tissues for histological analysis were fixed in 10% formalin (Fisher) for at least 7 days, tissues were embedded in paraffin, and 5-μm sections were prepared by the UNC histopathology core facility. To determine the extent of inflammation, sections were stained with hematoxylin and eosin (H&E) and scored in a blinded manner that is detailed in Text S1 in the supplemental material. Slides containing adjacent sections of lung tissue were stained with Martius scarlet blue (MSB) to visualize fibrin by the UNC histology core. Images were captured using an Olympus BX41 microscope with an Olympus DP71 camera.

RNA isolation, microarrays, quantitation of viral RNA species, full details of statistical analysis of gene expression data, and data dissemination are all discussed in Text S1 in the supplemental material.

SARS-CoV infection response network inference. To identify groups of host transcripts that showed coordinated regulation in response to infection with SARS-CoV, we applied WGCNA (21, 63). The WGCNA method detects signaling subnetworks or modules consisting of groups of genes that are highly connected according to a neighborhood proximity metric called the topological overlap (TO). TO quantifies the degree of shared network neighbors. Modules are represented as eigengenes by taking the first principal component of each set of module transcripts, which describe most of the variance in the module gene expression. We have adapted WGCNA into a workflow with three key steps: (i) *de novo* network construction, (ii) consensus network analysis, and (iii) network enrichment (see Fig. S4 in the supplemental material). The *de novo* network construction and the derivation of signaling modules are described in detail in Text S1 in the supplemental material. In addition to analysis of the individual doses, we utilized a consensus approach to identify modules present across both networks (see Fig. S4). Two nodes should be connected in a consensus network only if all of the input networks agree on that connection. We define the consensus network similarity between two nodes as the minimum of the input network similarities. This allows identification of regulatory differences between two networks, even when the resulting topology/modules are conserved.

Novel prioritization within network modules. We prioritized the statistically validated host response modules to identify signaling events that differed between doses at day 7 based on overall upregulation of the 10^5-PFU-dose treatment and differential module regulation when comparing treatments. Average $\log_2$ FCs were calculated across modules for each dose. Modules were labeled as upregulated at day 7 if the average $\log_2$ FC was greater than zero. A Δ average $\log_2$ FC was calculated by subtracting the average $\log_2$ FC for each dose at day 7. Network enrichment was then performed in two stages: functional enrichment using gene ontology (see Text S1 in the supplemental material for details) and connectivity enrichment. To aid in the prioritization of the candidates to be validated

within the modules, we examined the connectivity distribution relative to known canonical pathway membership within each module. We first identified canonical pathways that intersected with a given WGCNA module and then took the average TO connectivity between intersecting members. Ten thousand random samplings of sets of genes of the same size were used to derive a null distribution and determine if a given pathway was enriched for TO connectivity. This provides information regarding possible biological relevance to our putative candidates that had been ranked within the module based on their similarity to the eigengene.

Proteomics samples. For proteomics analysis, SARS-CoV- or mock-infected lung samples were collected and washed with 50 mM ammonium bicarbonate buffer, homogenized in 1 ml of 8 M urea in 50 mM ammonium bicarbonate buffer with glass beads for 60 s at 6,000 rpm, and then incubated for 1 h at room temperature. Samples were then centrifuged at 5,000 rpm to remove debris and immediately stored at −80°C. At each time point, analysis of individual mouse lungs provided intensity values for proteins derived from multiple peptides. The mean intensity (abundance) for each protein was then graphed as an average ($n = 5$ for infection, $n = 3$ for mock infection) for each group at each time point. Missing or absent values were not scored; however, if no value was observed in any of the samples at a time point, the sample was registered with a single 0, representing "not detected." Full details of the proteomics sample preparation methods are in the supplemental material.

SUPPLEMENTAL MATERIAL

Supplemental material for this article may be found at http://mbio.asm.org/lookup/suppl/doi:10.1128/mBio.00271-13/-/DCSupplemental.

Text S1, DOCX file, 0.1 MB.
Figure S1, TIF file, 13.9 MB.
Figure S2, TIF file, 13.9 MB.
Figure S3, TIF file, 13.9 MB.
Figure S4, TIF file, 1.3 MB.
Figure S5, TIF file, 13.9 MB.
Figure S6, TIF file, 13.9 MB.
Figure S7, TIF file, 13.9 MB.
Table S1, DOCX file, 0.1 MB.
Table S2, DOCX file, 0.1 MB.

ACKNOWLEDGMENTS

This work was supported by funds from the National Institute of Allergy and Infectious Diseases, National Institutes of Health, Department of Health and Human Services, contract number HHSN272200800060C, and from NIH/NCATS (5UL1RR024140). The proteomics work was performed in the Environmental Molecular Sciences Laboratory, a national scientific user facility sponsored by the Department of Energy's Office of Biological and Environmental Research and located at Pacific Northwest National Laboratory (PNNL), and used capabilities developed under efforts supported by the National Institute of General Medical Sciences (8 P41 GM103493-10). PNNL is operated by Battelle Memorial Institute for the DOE under contract number DE-AC05-76RLO1830.

REFERENCES

1. **Ksiazek TG, Erdman D, Goldsmith CS, Zaki SR, Peret T, Emery S, Tong S, Urbani C, Comer JA, Lim W, Rollin PE, Dowell SF, Ling AE, Humphrey CD, Shieh WJ, Guarner J, Paddock CD, Rota P, Fields B, DeRisi J, Yang JY, Cox N, Hughes JM, LeDuc JW, Bellini WJ, Anderson LJ, SARS Working Group.** 2003. A novel coronavirus associated with severe acute respiratory syndrome. N. Engl. J. Med. **348:**1953–1966.
2. **Lau SK, Woo PC, Li KS, Huang Y, Tsoi HW, Wong BH, Wong SS, Leung SY, Chan KH, Yuen KY.** 2005. Severe acute respiratory syndrome coronavirus-like virus in Chinese horseshoe bats. Proc. Natl. Acad. Sci. USA **102:**14040–14045.
3. **Christian MD, Poutanen SM, Loutfy MR, Muller MP, Low DE.** 2004. Severe acute respiratory syndrome. Clin. Infect. Dis. **38:**1420–1427.
4. **Zaki AM, van Boheemen S, Bestebroer TM, Osterhaus AD, Fouchier RA.** 2012. Isolation of a novel coronavirus from a man with pneumonia in Saudi Arabia. N. Engl. J. Med. **367:**1814–1820.
5. **Franks TJ, Chong PY, Chui P, Galvin JR, Lourens RM, Reid AH, Selbs E, McEvoy CP, Hayden CD, Fukuoka J, Taubenberger JK, Travis WD.** 2003. Lung pathology of severe acute respiratory syndrome (SARS): a study of 8 autopsy cases from Singapore. Hum. Pathol. **34:**743–748.
6. **Hwang DM, Chamberlain DW, Poutanen SM, Low DE, Asa SL, Butany J.** 2005. Pulmonary pathology of severe acute respiratory syndrome in Toronto. Mod. Pathol. **18:**1–10.
7. **Nicholls JM, Poon LL, Lee KC, Ng WF, Lai ST, Leung CY, Chu CM, Hui PK, Mak KL, Lim W, Yan KW, Chan KH, Tsang NC, Guan Y, Yuen KY, Peiris JS.** 2003. Lung pathology of fatal severe acute respiratory syndrome. Lancet **361:**1773–1778.
8. **Nicholls J, Dong XP, Jiang G, Peiris M.** 2003. SARS: clinical virology and pathogenesis. Respirology **8**(Suppl):S6–S8.
9. **Hui DS, Joynt GM, Wong KT, Gomersall CD, Li TS, Antonio G, Ko FW, Chan MC, Chan DP, Tong MW, Rainer TH, Ahuja AT, Cockram CS, Sung JJ.** 2005. Impact of severe acute respiratory syndrome (SARS) on pulmonary function, functional capacity and quality of life in a cohort of survivors. Thorax **60:**401–409.
10. **Ebbert JO, Limper AH.** 2005. Respiratory syncytial virus pneumonitis in immunocompromised adults: clinical features and outcome. Respiration **72:**263–269.
11. **Harms PW, Schmidt LA, Smith LB, Newton DW, Pletneva MA, Walters LL, Tomlins SA, Fisher-Hubbard A, Napolitano LM, Park PK, Blaivas M, Fantone J, Myers JL, Jentzen JM.** 2010. Autopsy findings in eight patients with fatal H1N1 influenza. Am. J. Clin. Pathol. **134:**27–35.
12. **Liem NT, Nakajima N, Phat LP, Sato Y, Thach HN, Hung PV, San LT, Katano H, Kumasaka T, Oka T, Kawachi S, Matsushita T, Sata T, Kudo K, Suzuki K.** 2008. H5N1-infected cells in lung with diffuse alveolar damage in exudative phase from a fatal case in Vietnam. Jpn. J. Infect. Dis. **61:**157–160.
13. **Bautista E, Chotpitayasunondh T, Gao Z, Harper SA, Shaw M, Uyeki TM, Zaki SR, Hayden FG, Hui DS, Kettner JD, Kumar A, Lim M, Shindo N, Penn C, Nicholson KG.** Clinical aspects of pandemic 200 influenza A (H1N1) virus infection. N. Engl. J. Med. **362:**1708–1719.
14. **Hoste EA, Roosens CD, Bracke S, Decruyenaere JM, Benoit DD, Vandewoude KH, Colardyn FA.** 2005. Acute effects of upright position on gas exchange in patients with acute respiratory distress syndrome. J. Intensive Care Med. **20:**43–49.
15. **De Smet R, Marchal K.** 2010. Advantages and limitations of current network inference methods. Nat. Rev. Microbiol. **8:**717–729.
16. **Langfelder P, Horvath S.** 2007. Eigengene networks for studying the relationships between co-expression modules. BMC Syst. Biol **1:**54. doi: 10.1186/1752-0509-1-S1-P54.
17. **Langfelder P, Zhang B, Horvath S.** 2008. Defining clusters from a hierarchical cluster tree: the Dynamic tree cut package for R. Bioinformatics **24:**719–720.
18. **Horvath S, Zhang B, Carlson M, Lu KV, Zhu S, Felciano RM, Laurance MF, Zhao W, Qi S, Chen Z, Lee Y, Scheck AC, Liau LM, Wu H, Geschwind DH, Febbo PG, Kornblum HI, Cloughesy TF, Nelson SF, Mischel PS.** 2006. Analysis of oncogenic signaling networks in glioblastoma identifies ASPM as a molecular target. Proc. Natl. Acad. Sci. U. S. A. **103:**17402–17407.
19. **Mariño-Ramírez L, Tharakaraman K, Bodenreider O, Spouge J, Landsman D.** 2009. Identification of cis-regulatory elements in gene co-expression networks using A-GLAM. Methods Mol. Biol. **541:**1–22.
20. **Mason MJ, Fan G, Plath K, Zhou Q, Horvath S.** 2009. Signed weighted gene co-expression network analysis of transcriptional regulation in murine embryonic stem cells. BMC Genomics **10:**327. doi: 10.1186/1471-2164-10-327.
21. **Zhang B, Horvath S.** 2005. A general framework for weighted gene co-expression network analysis. Stat. Appl. Genet. Mol. Biol. **4:**Article17. doi: 10.2202/1544-6115.1128.
22. **Roberts A, Deming D, Paddock CD, Cheng A, Yount B, Vogel L, Herman BD, Sheahan T, Heise M, Genrich GL, Zaki SR, Baric R, Subbarao K.** 2007. A mouse adapted SARS-coronavirus causes disease and mortality in BALB/c mice. PLoS Pathog. **3:**e5. doi: 10.1371/journal.ppat.0030005.
23. **Hattori N, Sisson TH, Xu Y, Desai TJ, Simon RH.** 1999. Participation of urokinase-type plasminogen activator receptor in the clearance of fibrin from the lung. Am. J. Physiol. **277:**L573–L579.
24. **Pardo A, Selman M.** 2006. Matrix metalloproteases in aberrant fibrotic tissue remodeling. Proc. Am. Thorac. Soc. **3:**383–388.
25. **Hatcher MA, Starr JA.** 2011. Role of tissue plasminogen activator in acute ischemic stroke. Ann. Pharmacother. **45:**364–371.

26. **Ding Y, Wang H, Shen H, Li Z, Geng J, Han H, Cai J, Li X, Kang W, Weng D, Lu Y, Wu D, He L, Yao K.** 2003. The clinical pathology of severe acute respiratory syndrome (SARS): a report from China. J. Pathol. **200:** 282–289.
27. **Rockx B, Sheahan T, Donaldson E, Harkema J, Sims AC, Heise M, Pickles RJ, Cameron M, Kelvin D, Baric RS.** 2007. Synthetic reconstruction of zoonotic and early human SARS-CoV isolates that produce fatal disease in aged mice. J. Virol. **81:**7410–7412.
28. **Langfelder P, Horvath S.** 2008. WGCNA: an R package for weighted correlation network analysis. BMC Bioinformatics **9:**559. doi: 10.1186/1471-2105-9-559.
29. **Van De Craen B, Declerck PJ, Gils A.** 2012. The biochemistry, physiology and pathological roles of PAI-1 and the requirements for PAI-1 inhibition in vivo. Thromb. Res. **130:**576–585.
30. **Nassar T, Yarovoi S, Fanne RA, Waked O, Allen TC, Idell S, Cines DB, Higazi AA.** 2011. Urokinase plasminogen activator regulates pulmonary arterial contractility and vascular permeability in mice. Am. J. Respir. Cell Mol. Biol. **45:**1015–1021.
31. **Idell S, James KK, Levin EG, Schwartz BS, Manchanda N, Maunder RJ, Martin TR, McLarty J, Fair DS.** 1989. Local abnormalities in coagulation and fibrinolytic pathways predispose to alveolar fibrin deposition in the adult respiratory distress syndrome. J. Clin. Invest. **84:**695–705.
32. **Wygrecka M, Jablonska E, Guenther A, Preissner KT, Markart P.** 2008. Current view on alveolar coagulation and fibrinolysis in acute inflammatory and chronic interstitial lung diseases. Thromb. Haemost. **99:** 494–501.
33. **Cesarman-Maus G, Hajjar KA.** 2005. Molecular mechanisms of fibrinolysis. Br. J. Haematol. **129:**307–321.
34. **Gajl-Peczalska K.** 1964. Plasma protein composition of hyaline membrane in the newborn as studies by immunofluorescence. Arch. Dis. Child. **39:**226–231.
35. **Peres e Serra A, Parra ER, Eher E, Capelozzi VL.** 2006. Nonhomogeneous immunostaining of hyaline membranes in different manifestations of diffuse alveolar damage. Clinics (Sao Paulo) **61:**497–502.
36. **Mallory GB, Jr..** 2001. Surfactant proteins: role in lung physiology and disease in early life. Paediatr. Respir. Rev. **2:**151–158.
37. **Subramanian A, Tamayo P, Mootha VK, Mukherjee S, Ebert BL, Gillette MA, Paulovich A, Pomeroy SL, Golub TR, Lander ES, Mesirov JP.** 2005. Gene set enrichment analysis: a knowledge-based approach for interpreting genome-wide expression profiles. Proc. Natl. Acad. Sci. U. S. A. **102:**15545–15550.
38. **Beissbarth T, Speed TP.** 2004. GOstat: find statistically overrepresented gene ontologies within a group of genes. Bioinformatics **20:**1464–1465.
39. **Frieman MB, Chen J, Morrison TE, Whitmore A, Funkhouser W, Ward JM, Lamirande EW, Roberts A, Heise M, Subbarao K, Baric RS.** 2010. SARS-CoV pathogenesis is regulated by a STAT1 dependent but a type I, II and III interferon receptor independent mechanism. PLoS Pathog. **6:**e1000849. doi: 10.1371/journal.ppat.1000849.
40. **Sheahan T, Morrison TE, Funkhouser W, Uematsu S, Akira S, Baric RS, Heise MT.** 2008. MyD88 is required for protection from lethal infection with a mouse-adapted SARS-CoV. PLoS Pathog. **4:**e1000240. doi: 10.1371/journal.ppat.1000240.
41. **Zhao J, Zhao J, Legge K, Perlman S.** 2011. Age-related increases in PGD(2) expression impair respiratory DC migration, resulting in diminished T cell responses upon respiratory virus infection in mice. J. Clin. Invest. **121:**4921–4930.
42. **Walters DM, Antao-Menezes A, Ingram JL, Rice AB, Nyska A, Tani Y, Kleeberger SR, Bonner JC.** 2005. Susceptibility of signal transducer and activator of transcription-1-deficient mice to pulmonary fibrogenesis. Am. J. Pathol. **167:**1221–1229.
43. **Chen CY, Lee CH, Liu CY, Wang JH, Wang LM, Perng RP.** 2005. Clinical features and outcomes of severe acute respiratory syndrome and predictive factors for acute respiratory distress syndrome. J. Chin. Med. Assoc. **68:**4–10.
44. **Yu H, Gao Z, Feng Z, Shu Y, Xiang N, Zhou L, Huai Y, Feng L, Peng Z, Li Z, Xu C, Li J, Hu C, Li Q, Xu X, Liu X, Liu Z, Xu L, Chen Y, Luo H, Wei L, Zhang X, Xin J, Guo J, Wang Q, Yuan Z, Zhang K, Zhang W, Yang J, Zhong X, Xia S, Li L, Cheng J, Ma E, He P, Lee SS, Wang Y, Uyeki TM, Yang W, Yang W.** 2008. Clinical characteristics of 26 human cases of highly pathogenic avian influenza A (H5N1) virus infection in China. PLoS One **3:**e2985. doi: 10.1371/journal.pone.0002985.
45. **Reynolds HN, McCunn M, Borg U, Habashi N, Cottingham C, Bar-Lavi Y.** 1998. Acute respiratory distress syndrome: estimated incidence and mortality rate in a 5 million-person population base. Crit. Care **2:**29–34.
46. **Tatebe K, Zeytun A, Ribeiro RM, Hoffmann R, Harrod KS, Forst CV.** 2010. Response network analysis of differential gene expression in human epithelial lung cells during avian influenza infections. BMC Bioinformatics **11:**170. doi: 10.1186/1471-2105-11-170.
47. **van Riel D, Leijten LM, van der Eerden M, Hoogsteden HC, Boven LA, Lambrecht BN, Osterhaus AD, Kuiken T.** 2011. Highly pathogenic avian influenza virus H5N1 infects alveolar macrophages without virus production or excessive TNF-alpha induction. PLoS Pathog. **7:**e1002099. doi: 10.1371/journal.ppat.1002099.
48. **Bruce SR, Atkins CL, Colasurdo GN, Alcorn JL.** 2009. Respiratory syncytial virus infection alters surfactant protein A expression in human pulmonary epithelial cells by reducing translation efficiency. Am. J. Physiol. Lung Cell. Mol. Physiol. **297:**L559–L567.
49. **Stinson SF, Ryan DP, Hertweck S, Hardy JD, Hwang-Kow SY, Loosli CG.** 1976. Epithelial and surfactant changes in influenzal pulmonary lesions. Arch. Pathol. Lab. Med. **100:**147–153.
50. **Burkhardt A.** 1989. Alveolitis and collapse in the pathogenesis of pulmonary fibrosis. Am. Rev. Respir. Dis. **140:**513–524.
51. **Dang CV, Bell WR, Kaiser D, Wong A.** 1985. Disorganization of cultured vascular endothelial cell monolayers by fibrinogen fragment D. Science **227:**1487–1490.
52. **Leavell KJ, Peterson MW, Gross TJ.** 1996. The role of fibrin degradation products in neutrophil recruitment to the lung. Am. J. Respir. Cell Mol. Biol. **14:**53–60.
53. **Zmijewski JW, Bae HB, Deshane JS, Peterson CB, Chaplin DD, Abraham E.** 2011. Inhibition of neutrophil apoptosis by PAI-1. Am. J. Physiol. Lung Cell. Mol. Physiol. **301:**L247–L254.
54. **Perrone LA, Plowden JK, García-Sastre A, Katz JM, Tumpey TM.** 2008. H5N1 and 1918 pandemic influenza virus infection results in early and excessive infiltration of macrophages and neutrophils in the lungs of mice. PLoS Pathog. **4:**e1000115. doi: 10.1371/journal.ppat.1000115.
55. **de Lang A, Baas T, Teal T, Leijten LM, Rain B, Osterhaus AD, Haagmans BL, Katze MG.** 2007. Functional genomics highlights differential induction of antiviral pathways in the lungs of SARS-CoV-infected macaques. PLoS Pathog. **3:**e112. doi: 10.1371/journal.ppat.0030112.
56. **Wu YP, Wei R, Liu ZH, Chen B, Lisman T, Ren DL, Han JJ, Xia ZL, Zhang FS, Xu WB, Preissner KT, de Groot PG.** 2006. Analysis of thrombotic factors in severe acute respiratory syndrome (SARS) patients. Thromb. Haemost. **96:**100–101.
57. **Prasad HB, Puranik SC, Kadam DB, Sangle SA, Borse RT, Basavraj A, Umarji PB, Mave V, Ghorpade SV, Bharadwaj R, Jamkar AV, Mishra AC.** 2011. Retrospective analysis of necropsy findings in patients of H1N1 and their correlation to clinical features. J. Assoc. Physicians India **59:** 498–500.
58. **Lim JH, Jono H, Komatsu K, Woo CH, Lee J, Miyata M, Matsuno T, Xu X, Huang Y, Zhang W, Park SH, Kim YI, Choi YD, Shen H, Heo KS, Xu H, Bourne P, Koga T, Yan C, Wang B, Chen LF, Feng XH, Li JD.** 2012. CYLD negatively regulates transforming growth factor-beta-signalling via deubiquitinating Akt. Nat. Commun. **3:**771. doi: 10.1038/ncomms1776.
59. **Lathem WW, Price PA, Miller VL, Goldman WE.** 2007. A plasminogen-activating protease specifically controls the development of primary pneumonic plague. Science **315:**509–513.
60. **Nakaya HI, Wrammert J, Lee EK, Racioppi L, Marie-Kunze S, Haining WN, Means AR, Kasturi SP, Khan N, Li GM, McCausland M, Kanchan V, Kokko KE, Li S, Elbein R, Mehta AK, Aderem A, Subbarao K, Ahmed R, Pulendran B.** 2011. Systems biology of vaccination for seasonal influenza in humans. Nat. Immunol. **12:**786–795.
61. **Querec TD, Akondy RS, Lee EK, Cao W, Nakaya HI, Teuwen D, Pirani A, Gernert K, Deng J, Marzolf B, Kennedy K, Wu H, Bennouna S, Oluoch H, Miller J, Vencio RZ, Mulligan M, Aderem A, Ahmed R, Pulendran B.** 2008. Systems biology approach predicts immunogenicity of the yellow fever vaccine in humans. Nat. Immunol. **10:**116–125.
62. **Deming D, Sheahan T, Heise M, Yount B, Davis N, Sims A, Suthar M, Harkema J, Whitmore A, Pickles R, West A, Donaldson E, Curtis K, Johnston R, Baric R.** 2006. Vaccine efficacy in senescent mice challenged with recombinant SARS-CoV bearing epidemic and zoonotic spike variants. PLoS Med. **3:**e525. doi: 10.1371/journal.pmed.0030525.
63. **Benjamini Y, Yekutieli D.** 2001. The control of the false discovery rate in multiple testing under dependency. Ann. Stat. **29:**1165–1188.